Computational Investigation of Micro Rotorcraft Near-Wall Hovering Aerodynamics

David Conal Robinson, Hoam Chung and Kris Ryan[1]

Abstract— Micro rotorcraft are considered a promising unmanned aerial platform owing to their high manoeuvrability and small footprint, which together allow for operation within very confined environments. This paper presents a computational investigation into a key challenge that limits micro rotorcraft performance within confined environments: Disturbance phenomena that occur due to aerodynamic interactions between rotors and nearby walls. The results of this study show that a micro rotor hovering near a wall will experience two wake asymmetry phenomena: Asymmetry in wake shape and asymmetry in vortex circulation strength. These asymmetry phenomena induce additional rotor force components that vary with rotor azimuthal angle. When averaged over time, these forces generate moments that present a disturbance large enough to have a significant adverse effect on micro rotorcraft blade flapping and attitude dynamics. Ultimately, this places the rotorcraft at a high risk of collision with the wall. This key result is fundamental to future design of disturbance observers and control systems that will be essential for future development of reliable confined environment micro rotorcraft systems.

I. INTRODUCTION

In search and rescue, surveillance and reconnaissance applications, unmanned micro rotorcraft are considered an especially promising platform owing to their high manoeuvrability and ability to operate within very confined environments [15]. Operation within very confined environments poses unique challenges, including aerodynamic interactions that occur between rotors and nearby surfaces, such as, walls, ceiling, ground, narrow passageways and other obstructions. These disturbances pose a barrier to the potential usefulness of micro rotorcraft as they have a significant adverse effect on stability; in order to develop micro rotorcraft systems that can reliably operate within confined environments, these disturbance effects must be understood and compensated for. As a first step toward achieving this goal, this paper outlines a computational study of a single main rotor micro rotorcraft hovering adjacent to a flat vertical wall. The aerodynamic disturbance effects present are analysed in detail and potential future implications of this study are also presented by postulating a robust disturbance observer based attitude control methodology. Such a robust control scheme is likely to be essential in order to ensure that micro rotorcraft platforms adhere to safety regulations that are likely to become ever stricter in coming years.

This paper is structured as follows: Sec. II outlines the computational methodology used; Sec. III outlines validation of the methodology; Sec. IV presents the key results ob-
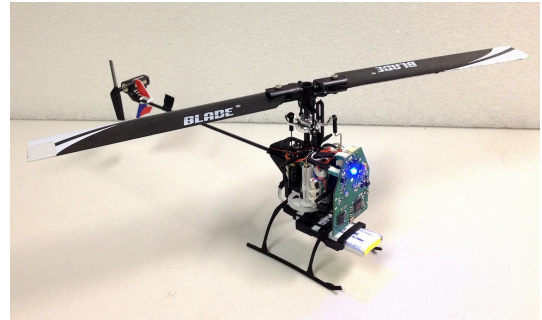
[1]David Conal Robinson, Hoam Chung and Kris Ryan are with the Faculty of Engineering, Monash University, Melbourne, Victoria, Australia

Fig. 1: *Single main rotor micro rotorcraft testbed*

tained; Sec. V discusses the key implications of this research; and Sec. VI contains conclusions and final remarks.

## II. COMPUTATIONAL FLUID DYNAMICS METHODOLOGY

A. Fluid Domain and Rotor Geometry

The rotor modelled in this research is based on a single main rotor micro helicopter testbed (see Fig. 1) that has been developed from the commercially available Blade Nano CPX helicopter. The blade section is modelled as a NACA0010 airfoil with a chord length, c, of 16.3mm, a radius, R, of 103.0mm and a blade collective pitch, α, of 7.5° (see Fig. 2 (a)). The body and tail rotor have initially been neglected from the model for simplification. The fluid domain surrounding the rotor is cylindrical in shape and consists of a near-field rotating region and a far-field stationary region (see Fig. 2 (b)). The far-field domain extends $10R$, $20R$ and $30R$ above, below and radially from the rotor hub respectively; the effect of the far-field geometry on flow characteristics will be examined further in Sec. III-B. The wall geometry is modelled as an immersed boundary [14] within the fluid domain.

B. Mesh

A tetrahedral grid with (with high density in the blade tip and wake regions) has been chosen as the preferred mesh for this research [20]. Additionally, prism layers with an exponential growth rate of 1.2 have been created at the blade surfaces in order to improve accuracy at the blade boundary layer regions. Element size has been automatically matched at the boundary between the prism layer region and the unstructured tetra region. Cross sections of the mesh showing the blade surface prism layers and the refinement throughout the wake region are provided in Figure 3. A comprehensive
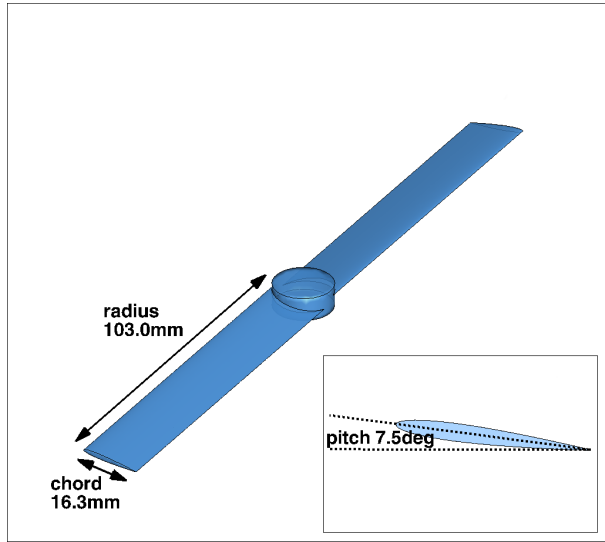
(a) Rotor
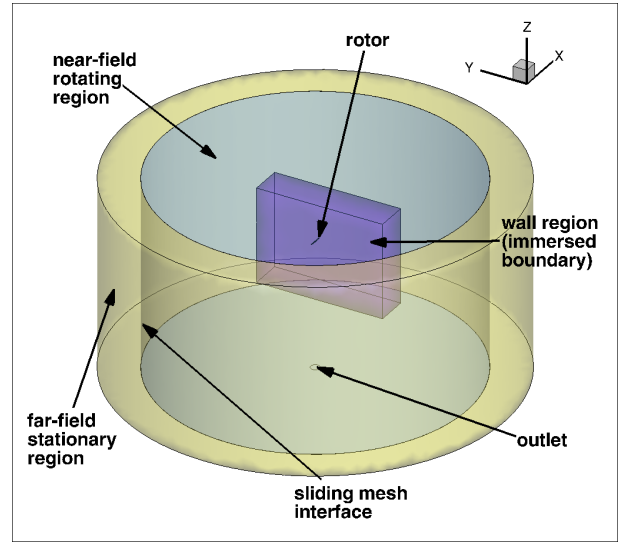
(b) Fluid domain including, stationary, rotating and immersed boundary regions

Fig. 2: *Domain geometry*

evaluation of mesh independence is outlined in Sec. III-A. ICEM CFD was employed in the construction of the computational grid.

C. Fundamental Governing Equations

Fundamentally, fluid mechanics are governed by the principles of mass and momentum conservation. Collectively, these principles are referred to as the Navier-Stokes equations; the solution to these equations forms the basis of computational fluid dynamics [3]. For this research, the flow is assumed to be incompressible (with the highest velocity components below Mach 0.3) and isothermal (because currently, only constant room temperature and pressure cases are being considered). Based on these assumptions, the Navier-Stokes equations can be simplified to

$$\rho(\frac{\partial \mathbf{v}}{\partial t} + \mathbf{v} \cdot \nabla \mathbf{v}) = -\nabla p + \mu \nabla^2 \mathbf{v} + \mathbf{f}, \qquad (1)$$

where ρ, v, p, f and μ are density, flow velocity, pressure, body forces and dynamic viscosity respectively. It has been assumed a-priori that the flow will be turbulent, with a quantity of kinetic energy measured at sub-grid scales. In order to model this effect, an averaged solution to Eq. 1 is used [3]. The solution to this Reynolds Averaged Navier Stokes (RANS) equation across the computational grid forms the basis of the CFD methodology in this research. Of particular interest in the RANS equation is the Reynolds stress term; due to the nonlinear nature of the Reynolds stress term a turbulence model is required in order to close the equation. Low Reynolds number rotor CFD studies from existing literature have provided evidence for the applicability of the Spalart-Allmaras model [18] [7]. Owing to its prevalence, as well as its evaluation in a comprehensive turbulence model study (outlined in Sec. III-C), the Spalart-Allmaras turbulence model has been chosen for use in this research. Because it only requires one additional equation to be solved per iteration it is significantly less computationally intensive than commonly used two-equation k-ϵ and k-ω based models.

The effect of a wall on the flow field is modelled by using the wall region to define the geometry of an immersed boundary. Essentially, flow velocity is brought to rest at the wall interface region through the addition of a momentum source term, calculated as

$$S_x = -C(U_x - U_{x,immersed}), \qquad (2a)$$
$$S_y = -C(U_y - U_{y,immersed}), \qquad (2b)$$
$$S_z = -C(U_z - U_{z,immersed}), \qquad (2c)$$

where S_x, S_y, S_z are momentum source terms, C is the immersed source coefficient, U_x, U_y, U_z are the flow momentum terms and $U_{x,immersed}$, $U_{y,immersed}$, $U_{z,immersed}$ are the specified immersed boundary momentum terms. The immersed boundary method is especially flexible because it allows for a solid object of any arbitrary shape to be *'immersed'* at any location within the fluid domain without requiring any changes to the background mesh.

The far-field boundary conditions have been prescribed using the source-sink method, first postulated by [19]. This method allows fluid to enter the domain through the far boundaries toward a sink located at the rotor hub. Flow exits the domain through an outlet set to the free stream pressure located directly below the rotor. The prescribed inlet velocity profile at the far-field boundary is derived from blade momentum theory as [19]

$$W_{in} = \frac{V_{tip}}{4}\sqrt{\frac{C_T}{2}}\frac{R^2}{d^2}, \qquad (3)$$

where W_{in}, V_{tip}, C_T, R, d are inlet flow velocity, rotor tip velocity, thrust coefficient, rotor radius and distance from the
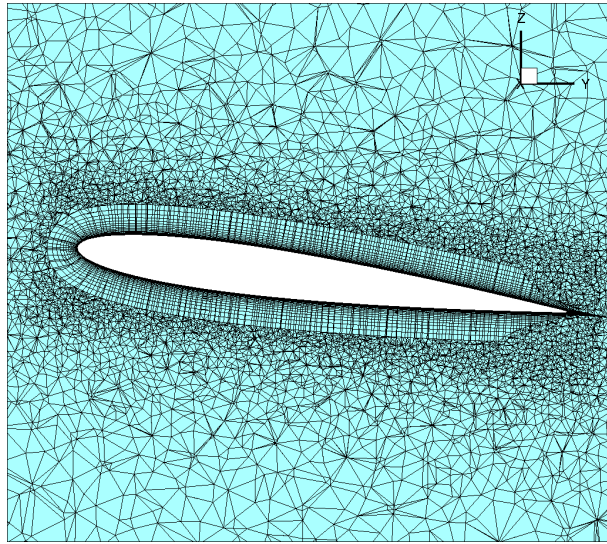
(a) Cross section of mesh through YZ-axis showing blade surface prism layers
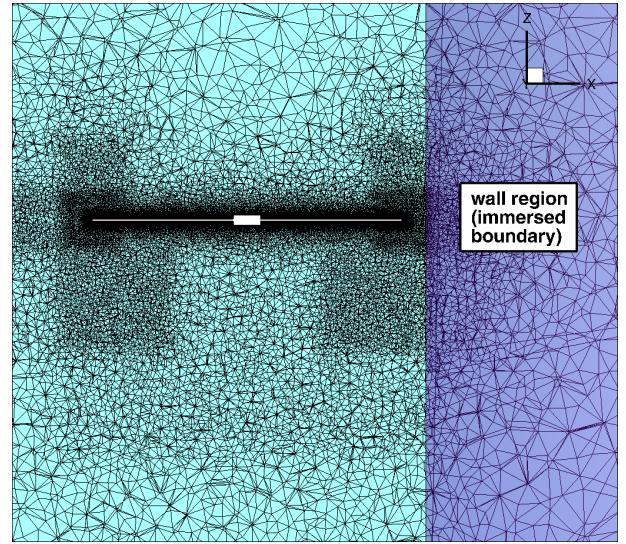
(b) Cross section through XZ-axis showing blade-tip and rotor wake refinement regions

Fig. 3: *Mesh cross section*

sink respectively. The inlet velocity profile is updated every time-step using the value of C_T calculated at the previous time-step.

D. Solver Scheme

To maximise solver accuracy, a second order implicit solver is used to numerically obtain the solution across the flow field. The solver iterates until RMS residual error converges to below 10^{-5}. With each time step, the rotating region rotates by 1.8^o using a moving mesh model. The results presented in this research are obtained using the AN-SYS CFX solver and the Monash Sun Grid high performance computing cluster.

III. VALIDATION OF COMPUTATIONAL METHODOLOGY

A. Mesh Independence Study

A mesh independence study has been conducted in order to ensure that the CFD results obtained are independent of the mesh resolution. Simulations were run with a separation of $2c$ between the rotor disk and wall using three meshes with varying levels of refinements. The mesh refinement for each mesh is defined by a global mesh refinement scaling factor, M. For the three meshes used, $M = 1.5, 2.0, 2.5$. A summary of the mesh refinement used in each of the three meshes is provided in Tab. I.

To quantify the error associated with each mesh, a Richardson extrapolation [17] is used to estimate the actual solution value by eliminating lower order error terms using the following equation

$$\phi \approx \phi_{n+1} + \frac{\phi_{n+1} - \phi_n}{(\frac{h_{n+1}}{h_n})^2 - 1}, \qquad (4)$$

where, ϕ is the actual solution estimate, ϕ_n is the solutions of mesh n and h_n is a representative cell dimension, calculated by

$$h_n = \left[\frac{1}{N_n} \sum_{i=1}^{N_n} (V_{n,i}) \right]^{\frac{1}{3}}, \qquad (5)$$

where N_n is the number of elements in the nth mesh and $V_{n,i}$ is the volume of the ith element of the nth mesh. Using this method, all of the solutions attained as part of the mesh independence study are combined to eliminate error terms up to (and including) the 4th order. By comparing the solution obtained using each mesh with the Richardson extrapolation solution estimate, the error up to the 4th order for each mesh can be calculated. A summary of RMS percentage lift error and peak percentage error lift vs mesh refinement is included in Tab. I. From this error data it is clear that error magnitude exhibits monotonic convergence as mesh refinement is increased. Based on this result, it was decided that the RMS error of less than 1% and peak error of less that 2% provided by the $M = 2.0$ mesh provided suitable of accuracy for this research.

B. Domain Size Study

In order to ensure that the results obtained were independent of the domain size, two additional simulations (with the wall gap set at $2c$) were run with the domain size increased separately by a factor of two in the vertical and radial directions. The effects of varied domain size on blade lift is summarised in Tab. II, where the error terms are measured relative to the nominal domain results. The results of the domain size study show that peak error (measured relative to the nominal domain) remains below 1%, as such, the nominal domain size has been deemed acceptable for performing all production simulations in this research.

TABLE I: Mesh independence study

global mesh refinement factor, M	No. elements	No. nodes	h	% RMS lift error	% peak lift error
1.5	$3.69e^6$	$9.14e^5$	$2.93e^{-2}$	1.43	2.81
2.0	$6.94e^6$	$1.73e^6$	$2.37e^{-2}$	0.99	1.87
2.5	$1.26e^7$	$3.26e^7$	$1.95e^{-2}$	0.63	1.24

TABLE II: Domain size study

	height (R)	radius (R)	% RMS lift error	% peak lift error
nominal domain	30	30	-	-
domain z	60	30	0.18	0.39
domain r	30	60	0.48	0.85

TABLE III: Turbulence model study

turbulence model	y-moment (Nm)	x-moment (Nm)
k-ϵ [2]	$3.34e^{-4}$	$-1.57e^{-4}$
k-ω [21]	$3.35e^{-4}$	$-1.49e^{-4}$
k-ω baseline [12]	$3.29e^{-4}$	$-1.51e^{-4}$
k-ω shear stress transport [12]	$3.37e^{-4}$	$-1.48e^{-4}$
Spalart-Allmaras [18]	$3.31e^{-4}$	$-1.50e^{-4}$

C. Turbulence Model Study

Despite the Spalart-Allmaras model's use in the literature for micro rotor research [7] it was nonetheless deemed necessary to compare its performance with other models in order the validate its applicability for this research. A summary of the *x-moment* and *y-moment* (about the rotor disk) for several different turbulence models is provided in Tab. III. The table shows that there is good agreement between the Spalart-Allmaras model and the k-ω based models. The Spalart-Allmaras model has been deemed appropriate for this research based on this agreement, it's usage in the literature, and its low computational requirements. Note that turbulence modelling will also be validated experimentally as part of future work.

IV. RESULTS

Using the methodology outlined in Sec. II, CFD simulations have been run with no wall in the fluid domain and with a wall placed between $2c$ and $10c$ from the rotor disk (increasing in increments of $2c$) and with the blade rotating in a clock-wise direction (when viewed from above) at 3 200 RPM. The resulting wakes have been compared between the no-wall case and the $2c$ near-wall case in order to identify the key flow characteristics associated with a near-wall hovering micro rotor. In Fig. 4 velocity magnitude contours are compared at cross sections through the rotor.

The no-wall case exhibits a radially contracting wake that is consistent with hovering low blade-tip Reynolds number rotors at hover from the literature [16], [8]. Note that the wake dissipates more than would be expected for a full-scale helicopter rotor, owing to the micro rotor's low blade-tip Reynold's number (50 000). In contrast, the near-wall case has a wake that exhibits radial contraction at the far-wall side of the rotor but very little radial contraction at the near-wall side of the rotor disk. This is consistent with what is expected from the Navier-Stokes equations as the presence of the wall significantly reduces the component of velocity normal to the wall; instead, in order to maintain conservation of momentum, the flow velocity must remain predominantly parallel to the wall.

The altered wake shape is further evident in Fig. 5, where the helical blade tip wake vortices (represented by vorticity magnitude isosurfaces) are shown to contract radially for the no-wall case, however, there is very little radial contraction for the near-wall case at the near-wall side of the rotor disk. The change in shape of the rotor wake is very significant as the location and strength of the helical vortex wake affects the flow velocity at the blade, as governed by the Biot-Savart Law [9]. The nature of the wake asymmetry becomes clearer still when vorticity magnitude cross sections are analysed in Fig. 6 (arrows have been superimposed over the plots to indicate the general direction of wake convection). Once again, the no-wall case exhibits a radially contracting symmetrical wake, with both vortex wakes of equal strength. In contrast, the near-wall case exhibits two independent asymmetry phenomena: asymmetry in wake shape (indicated by the superimposed arrows in Fig. 6); and asymmetry in vortex circulation strength (most pronounced in Fig. 6 (e)).

Wake shape asymmetry is least pronounced in the *y*-direction (parallel to the wall), as show in Fig. 6 (f). This is because the fluid flow is not inhibited in the plane parallel to the wall and, therefore, radial wake contraction occurs readily in this plane. In contrast, there is clear asymmetry in the wake shape as the blade tip passes the wall in Fig. 6 (c,d,h). This is because fluid has been prevented from entering the rotor
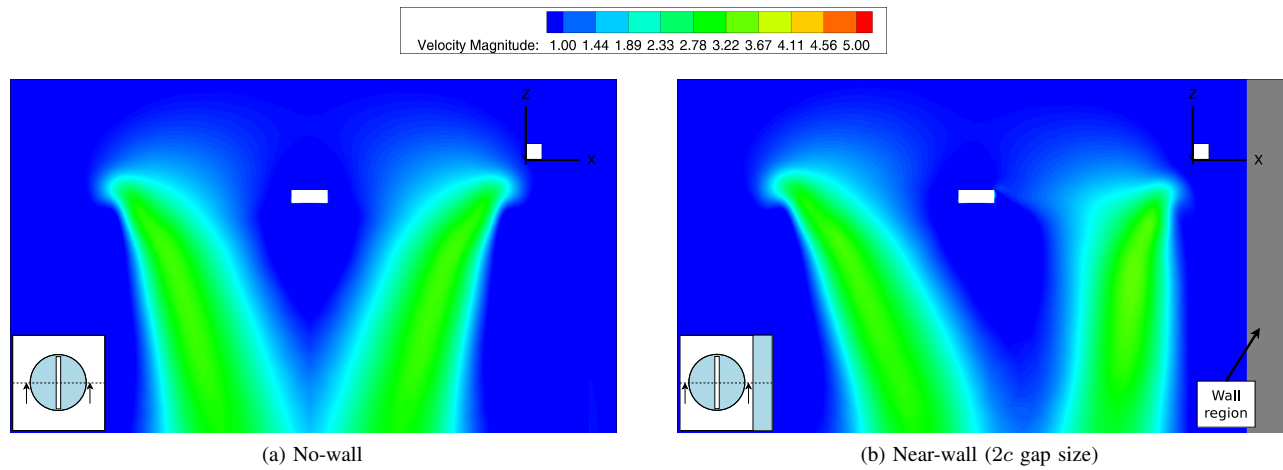
Velocity Magnitude: 1.00 1.44 1.89 2.33 2.78 3.22 3.67 4.11 4.56 5.00

(a) No-wall

(b) Near-wall (2c gap size)

Fig. 4: *Cross section of velocity contours (ms^{-1})*
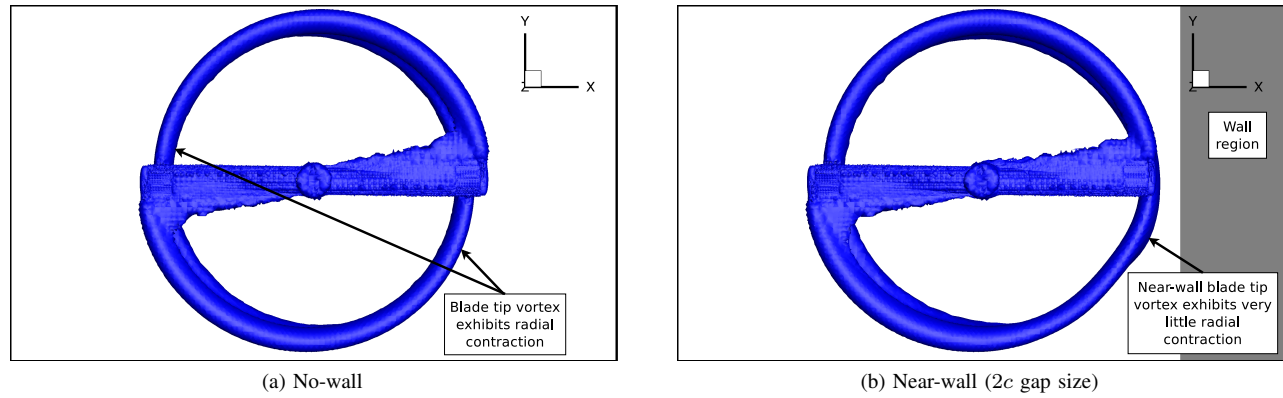

(a) No-wall

(b) Near-wall (2c gap size)

Fig. 5: *Vorticity magnitude isosurfaces (viewed from above)*

disk from the direction normal to the wall; as such, fluid must enter the rotor disk from above (parallel to the wall) and the wake convects downwards with little radial contraction as a result.

Further to this, asymmetry in vortex strength can also be explained by the presence of the wall. As the blade tip, approaches the wall (Fig. 6 (g, h)) the vortex strength remains close to symmetrical at either side of the wake. This is because there is a large volume of fluid to be drawn into the wake as the blade approaches the wall. In contrast, immediately after the blade tip has passed the wall, the presence of the wall inhibits fluid from being drawn into the wake. As a result, vortex circulation strength reduces significantly immediately after the blade tip passes the wall causing asymmetry in vortex circulation strength across the rotor disk (Fig. 6 (d, e)).

Asymmetry in wake shape is expected to result in reaction forces in the horizontal direction at the rotor hub. This is confirmed by analysis of non-dimensionalised rotor hub forces,

$$F^* = \frac{F}{mg}, \qquad (6)$$

where F^*, F and mg are non-dimensionalised force, force and rotorcraft weight respectively. Plots of F^* vs rotor

azimuthal angle, θ (measured in a clockwise direction, where $\theta = 0$ when the blade tip is nearest the wall) in the x and y directions (where the x-axis is horizontal and normal to the wall and the y-axis is horizontal and parallel to the wall) are provided Fig. 7. For the no-wall case, the horizontal forces at the rotor hub are zero because the wake is symmetrical. For $\theta = 90^o/270^o$ (Fig. 6 (c)), x-force is large and directed toward the wall, because there is significant asymmetry in wake shape in the x-direction. In contrast, the y-force is close to zero at $\theta = 90^o/270^0$ because the wake shape is close to symmetrical (Fig. 6 (f)). Note, also, that the x and y forces fluctuate as θ varies. This gives a time averaged non-dimensionalised x-force of $F^* = -2.3e^{-3}$ and y-force of $F^* = 0$ for 2c wall gap. The wake shape also has a small effect on the lift force (in the z-direction). However, the lift generated by a blade is dominated by vortex circulation strength. This is confirmed by the plot of lift force (non-dimensionalised by rotorcraft weight) for a single blade provided in Fig. 8. Once again, the no-wall case exhibits and constant lift force, owing to vortex circulation symmetry. For the near-wall case, at $\theta = 0^o$-180°, the vortex circulation strength is weaker that the opposite side of the wake and this corresponds to a reduction in lift force (with a minimum value of $F^* = 0.48$ occurring at $\theta = 180^o$). At $\theta = 180^o$-
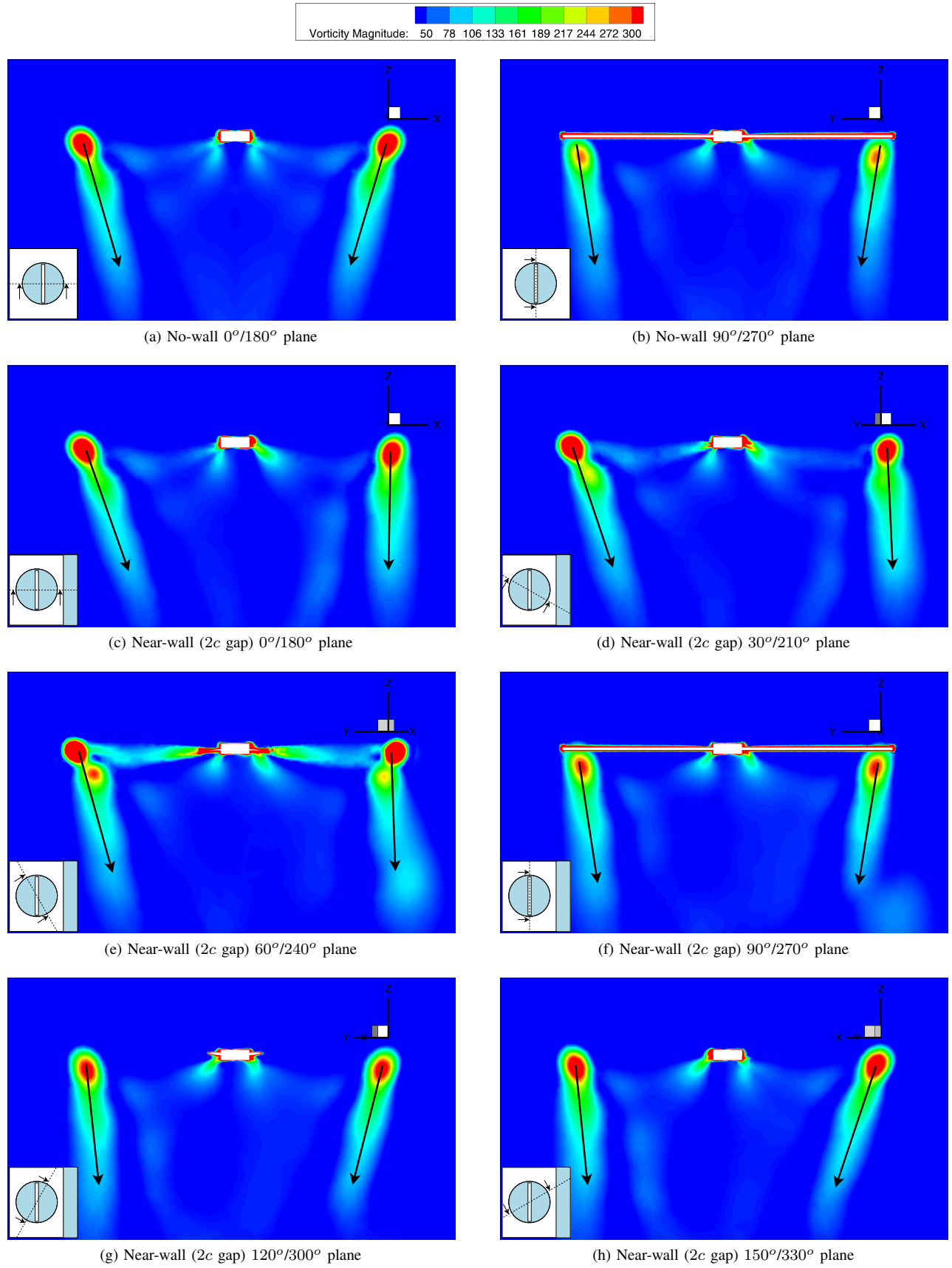
(a) No-wall $0^o/180^o$ plane

(b) No-wall $90^o/270^o$ plane

(c) Near-wall ($2c$ gap) $0^o/180^o$ plane

(d) Near-wall ($2c$ gap) $30^o/210^o$ plane

(e) Near-wall ($2c$ gap) $60^o/240^o$ plane

(f) Near-wall ($2c$ gap) $90^o/270^o$ plane

(g) Near-wall ($2c$ gap) $120^o/300^o$ plane

(h) Near-wall ($2c$ gap) $150^o/330^o$ plane

Fig. 6: *Cross sections of vorticity magnitude contours (s^{-1})*

(b) *X*-direction

Fig. 8: *F* acting on a single blade in z-direction vs θ
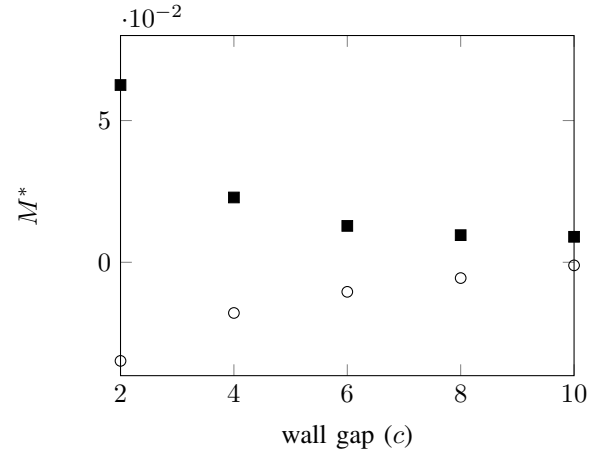
Fig. 9: *Plot of moment vs wall gap (square marker: moments about y-axis; circle marker: moments about x-axis)*
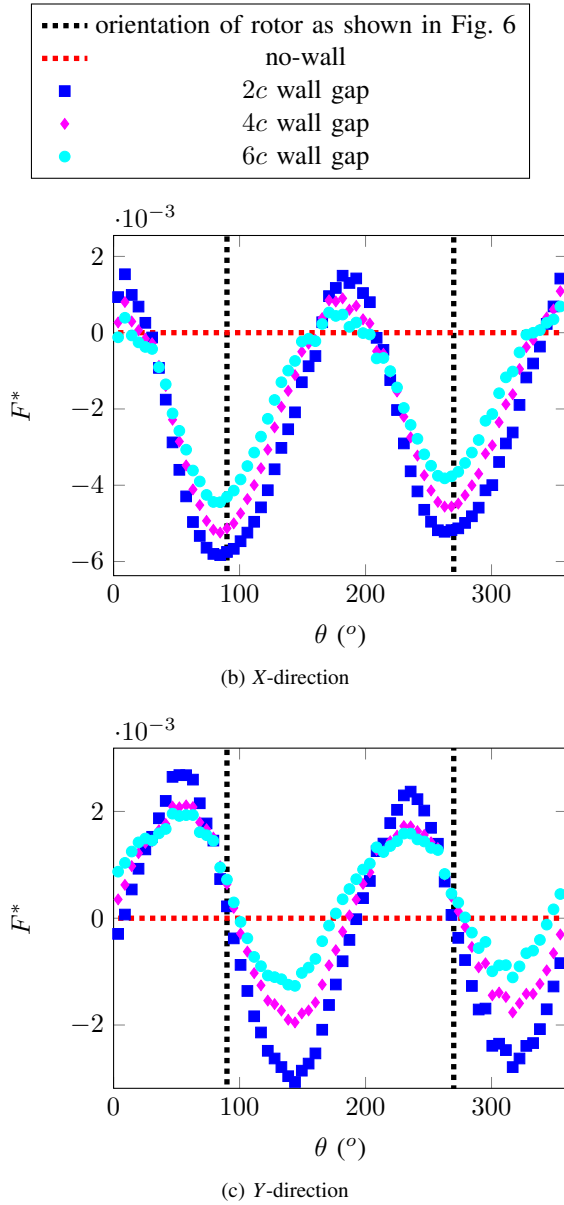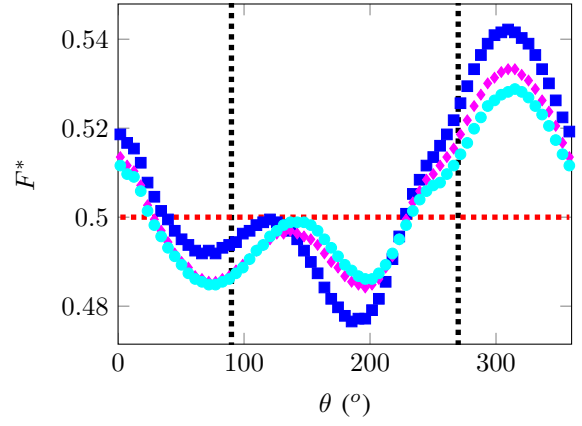

(c) *Y*-direction

Fig. 7: *Plots of F* vs θ*

360°, the stronger vortex circulation strength increases and this corresponds to a stronger lift force (with a peak value of $F^* = 0.54$ occurring at $\theta = 310^o$. Like the horizontal force at the rotor hub, lift force at the blade will also vary significantly with θ. For both the horizontal and vertical forces, Fig. 7 and Fig. 8 indicate an inverse relationship between wall gap size and range of force variation.

Due to lift imbalance across the rotor disk generated by the varying lift force shown in Fig. 8, significant moments about the *x*- and *y*-axes will act on the micro rotorcraft. Time averaged moments about the *x*- and *y*-axes are plotted in Fig. 9, where moments are non-dimensionalised by

$$M^* = \frac{M}{WG\ mg}, \qquad (7)$$

where M^*, M, WG, mg are non-dimensionalised moment,

moment, wall gap distance and rotorcraft weight respectively. As expected, the magnitude of the time averaged moments acting at the rotor hub asymptote toward 0 as wall gap increases; as wall gap decrease, there is a significant rapid increase in moment magnitude. Note that, due to gyroscopic precession, these moments will act on the body of the rotorcraft 90° after acting on the rotor disk. Additionally, although not shown in this paper, forces at the rotor hub in the *x* and *y* directions will generate smaller moments acting on the body of the rotorcraft. This relationship between wall-gap and perturbation moments acting on the rotorcraft is a key finding of this research; and comprehensive understanding of this relationship is vital for development of autonomous control system that can avoid catastrophic collisions with walls by compensating for near-wall perturbation moments.

V. DISCUSSION

As an extension of the results presented in Sec. IV, it is important to consider a methodology for compensating for the disturbances generated by near-wall aerodynamic effects. One method that has been investigated for improving control performance in the presence of disturbances is the use of *disturbance observer* based control systems [6], [11].

A disturbance observer improves regulation performance in the presence of unmodelled uncertainty by driving the system and disturbance dynamics to the nominal system dynamics [6]. The result is that the aircraft, disturbance and disturbance observer dynamics combine to behave like the nominal aircraft dynamics. This means that a controller that is designed to stabilise nominal aircraft dynamics can still provide good performance in the presence of disturbances if it is implemented in conjunction with a disturbance observer. A disturbance observer based controller is especially useful for systems where it is very difficult to directly measure the magnitude of a disturbance; a block diagram showing the general form of a disturbance observer based control system is provided in Fig. 10. This method has previously been implemented by [11] to control attitude of a small-scale rotorcraft in the presence of wind gust disturbances. In principle, a similar methodology, postulated in this section, can be used to control attitude of micro rotorcraft hovering adjacent to a wall.

A disturbance observer could be designed using a methodology postulated by [1]. First, the disturbance generated by aerodynamic interaction between the rotor and the wall will be modelled as a linear system

$$\dot{\varepsilon} = A_d \varepsilon, \tag{8a}$$
$$d = C_d \varepsilon, \tag{8b}$$

where ε, d, A_d, C_d are the disturbance state vector, observable disturbance state vector and state matrices respectively. The disturbance dynamics will be determined by taking a Taylor series expension of the moment vs wall gap relationship from Fig. 9.

The disturbance observer also requires a model of micro rotorcraft attitude dynamics. The model used will be a linear time-invariant representation of attitude dynamics and blade flapping dynamics [13];

$$
\begin{bmatrix} \dot{p} \\ \dot{q} \\ \tau_f \dot{a} \\ \tau_f \dot{b} \end{bmatrix} =
\begin{bmatrix} 0 & 0 & 0 & L_b \\ 0 & 0 & M_a & 0 \\ 0 & -\tau_f & -1 & 0 \\ -\tau_f & 0 & 0 & -1 \end{bmatrix}
\begin{bmatrix} p \\ q \\ a \\ b \end{bmatrix}
$$
$$
+ \begin{bmatrix} 0 & 0 \\ 0 & 0 \\ 0 & A_{lon} \\ B_{lat} & 0 \end{bmatrix}
\begin{bmatrix} \delta_{lat} \\ \delta_{lon} \end{bmatrix}
$$
$$
+ \begin{bmatrix} 0 & 0 \\ 0 & 0 \\ 0 & 1 \\ 1 & 0 \end{bmatrix} d, \tag{9}
$$

where p, q, a, b, M_a, L_b, τ_f, B_{lat}, A_{lon} are roll rate, pitch rate, lateral flapping, longitudinal flapping, lateral flapping derivative, longitudinal flapping derivatives, flapping time constant, lateral cyclic and longitudinal cyclic respectively. [13], [4] have previously shown that the assumption of linear attitude dynamics is valid for hovering flight. Frequency
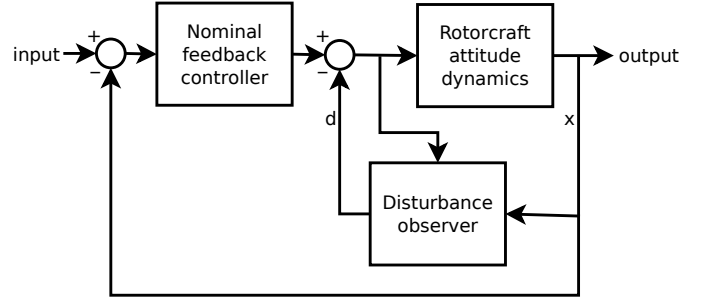

Fig. 10: *Block diagram structure of a disturbance observer based control system*

domain parametric system identification will be used to identify the unknown parameters in the attitude dynamics model [5].

By rewriting Eq. 9 in the general form

$$\dot{x} = Ax + Bu + Dd, \tag{10}$$

where A, B, D, x, u, d are the state matrix, input matrix, disturbance matrix, state vector, input vector and disturbance vector respectively, then the general form of a basic disturbance observer (as derived by [1]) can be postulated as

$$\dot{\hat{\varepsilon}} = A_d \hat{\varepsilon} + L(\dot{x} - Ax - Bu - D\hat{d}), \tag{11a}$$
$$\hat{d} = C_d \hat{\varepsilon}, \tag{11b}$$

where L is the disturbance observer gain matrix. Note that the disturbance observer is designed using experimentally identified nominal attitude dynamics and numerically identified near-wall disturbance dynamics.

By calculating the disturbance estimate, $\hat{d}$, from Eq. 11 and using the control structure shown in Fig. 10, a disturbance observer control system can be implemented. Additionally, it is worth noting that factors such as flight data noise, first order approximation of flapping dynamics, rotor orientation relative to the wall, tail rotor aerodynamics will introduce uncertainty into the system and disturbance models. To ensure robust stability in the presence of this unmodelled uncertainty, it will be necessary to implement model based control schemes such as Linear Quadratic Regulation (LQR), sliding mode, H_2, H_∞, Model Predictive Control (MPC), etc can potentially be used to design the controller block. In principle, this novel application of disturbance observer based control will maintain robust control of a micro rotorcraft hovering near a flat wall. Further to this, the disturbance estimate will be calculated using only a priori models and the rotorcrafts internal states (measured using an inertial navigation system). Fundamentally, this will allow for a wall to *observed* without the need for any active exteroceptive sensor, such as infra-red or laser range finders. This is particularly significant for micro scale rotorcraft where available payload and power are severely constrained by the aircrafts size. Ultimately, a disturbance observer based micro rotorcraft control system, designed using the numerical

and analytical methodology outlined in this paper, will be able to autonomously detect and robustly compensate for the presence while having no detrimental effect on the payload and flight-time of the aircraft.

VI. CONCLUSIONS AND FUTURE WORK

In conclusion, key findings of this research are as follows:

- The wake of a micro rotorcraft hovering adjacent to a vertical wall will be asymmetrical in shape, with the far-wall side of the wake contracting radially and the near-wall side of the wake moving predominantly parallel to the wall. This wake asymmetry creates horizontal forces acting at the rotor hub that vary with rotor azimuthal angle.

- The wake of a micro rotorcraft hovering adjacent to a vertical wall has asymmetry in vortex circulation strength. This creates lift forces at the blade that vary with rotor azimuthal angle.

- Varying components of force acting on the rotor due to aerodynamic interactions with the wall generate time averaged moments acting at the rotor hub. These moments reduce in magnitude monotonically as gap size between the rotor disk and wall increases. When near to the wall, these moments are large enough in magnitude to have a significant adverse effect on micro rotorcraft stability.

- A disturbance observer based control system has been postulated that will be able to detect the distance from and orientation relative to a wall and will be able to provide a robust control correction in order to ensure that a stable attitude can be maintained when hovering near to a wall.

As part of proposed future work, the CFD results outlined in this paper will be validated by comparison with experimental results and analytic Free Vortex Method [10] results. Following this, the control scheme postulated in Sec. V will be implemented, first in simulation, and finally experimentally in a motion capture laboratory.

REFERENCES

[1] Wen-Hua Chen. Disturbance observer based control for nonlinear systems. *IEEE/ASME Transactions on Mechatronics*, 9(4):706–710, 2004.

[2] Kuei-Yuan Chien. Predictions of channel and boundary-layer flows with a low-reynolds-number turbulence model. *AIAA Journal*, 20(1):33–38, 1982.

[3] Joel H. Ferziger and Milovan Peric. *Computational Methods for Fluid Dynamics*. Springer, 2002.

[4] J. Grauer, J. Conroy, J. Hubbard, J. Humbert, and D. Pines. System identification of a miniature helicopter. *Journal of Aircraft*, 46(4):1260–1269, 2012/12/05 2009.

[5] Morelli E. Klein, V. *Aircraft System Identification Theory and Practice*. American Institute of Aeronautics and Astronautics, Inc., 2006.

[6] SangJoo Kwon and Wan Kyun Chung. *Pertubation Compensator based Robust Tracking Control and State Estimation of Mechanical Systems*. Springer, 2004.

[7] Vinod K. Lakshminarayan. *Computational Investigation of Micro-Scale Coaxial Rotor Aerodynamics in Hover*. PhD thesis, University of Maryland, 2009.

[8] Vinod K. Lakshminarayan and James D. Baeder. Computational investigation of micro hovering rotor aerodynamics. *Journal of the American Helicopter Society*, 55:022001–1–022001–25, 2010.

[9] J. Gordon Leishman. *Principles of Helicopter Aerodynamics*. Cambridge University Press, 2006.

[10] J. Gordon Leishman, Mahendra J. Bhagwat, and Ashish Bagai. Free-vortex filament methods for the analysis of helicopter rotor wakes. *Journal of Aircraft*, 39(5):759–775, 2002.

[11] Cunjia Liu, Wen-Hua Chen, and John Andrews. Tracking control of small-scale helicopters using expelicit nonlinear mpc augmented with disturbance observers. *Control Engineering Practice*, 20:258–268, 2012.

[12] F. R. Menter. Two-equation eddy-viscosity turbulence models for engineering applications. *AIA Journal*, 32(8):1598–1605, 1994.

[13] Bernard Mettler, Mark Tischler, and Takeo Kanade. System identification modeling of a small-scale unmanned rotorcraft for flight control design. *Journal of the American Helicopter Society*, 47:50–63, 2002.

[14] Rajat Mittal and Gianluca Iaccarino. Immersed boundary methods. *Annual Review of Fluid Mechanics*, 37:239–261, 2005.

[15] Darryll Pines and Felipe Bohorquez. Challenges facing future micro-air-vehicle development. *Journal of Aircraft*, 43:290–305, 2006.

[16] Manikandan Ramasamy, Bradley Johnson, and J. Gordon Leishman. Understanding the aerodynamics efficiency of a hovering micro-rotor. *Journal of the American Helicopter Society*, 53(4):412–428, 2008.

[17] L. F. Richardson. The approximate arithmetical solution by finite differences of physical problems including differential equations, with an application to the stresses in a masonry dam. *Philosophical Transactions of the Royal Society of London.*, 210:307–357, 1911.

[18] P. Spalart and S. Allmaras. A one-equation turbulence model for aerodynamic flows. In *30th Aerospace Sciences Meeting and Exhibit*, 1992.

[19] G. R. Srinivasan, V. Raghavan, E. P. N. Duque, and W. J. McCroskey. Flowfield analysis of modern helicopter rotors in hover by navier-stokes method. *Journal of the American Helicopter Society*, 38(3):3–13, 1993.

[20] V. Venkatakrishnan. Perspective on unstructured grid flow solvers. *AIAA Journal*, 34(3):533–547, 1996.

[21] David C. Wilcox. Formulation of the k-omega turbulence model revisited. *AIA Journal*, 46(11):2823–2838, 2008.